Materials Today Physics 41 (2024) 101346

Contents lists available at ScienceDirect

Materials Today Physics

journal homepage: www.journals.elsevier.com/materials-today-physics

Thermal conductivity reduction in highly-doped cubic SiC by phonon-defect and phonon-electron scattering

Guijian Pang [a], Fanchen Meng [b], Yani Chen [a], Ankita Katre [c], Jesús Carrete [d], Bonny Dongre [e], Georg K.H. Madsen [e], Natalio Mingo [f], Wu Li [g,a,*]

[a] Institute for Advanced Study, Shenzhen University, Shenzhen, 518060, China
[b] Research Computing and Data, Clemson Computing and Information Technology, Clemson University, Clemson, SC, 29634, USA
[c] Department of Scientific Computing, Modeling and Simulation, SP Pune University, Pune, 411007, India
[d] Instituto de Nanociencia y Materiales de Aragón (INMA), CSIC-Universidad de Zaragoza, E-50009, Zaragoza, Spain
[e] Institute of Materials Chemistry, TU Wien, A-1060, Vienna, Austria
[f] Université Grenoble-Alpes, CEA, LITEN, 17 rue des Martyrs, 38054, Grenoble, Cedex 9, France
[g] Eastern Institute for Advanced Study, Eastern Institute of Technology, 315200, Ningbo, China

A B S T R A C T

We calculate the thermal conductivity (κ) of highly N- and B-doped cubic silicon carbide (SiC) with defect concentrations (C_{def}) from 10^{16} to 10^{21} cm^{-3} and compare the relative importance of the extrinsic phonon-electron and phonon-defect scattering mechanisms. Whereas phonon-electron scattering dominates over phonon-defect scattering at low C_{def} up to about 10^{20} cm^{-3} at room temperature in N-doped SiC, phonon-defect scattering determines the thermal conductivity reduction in the B-doped case. This strong contrast between the electron- and hole-doped cases is related to the much higher ionization energy of B acceptors as compared to that of N donors, and to the resonant scattering caused by B substitution, not present for the N impurity. The similar features can be found in hexagonal phase 4H–SiC. Our results highlight the importance of considering the phonon-electron scattering mechanism together with other phonon scattering processes when calculating the thermal conductivity of doped semiconductors.

1. Introduction

Silicon carbide (SiC) has applications in various fields ranging from thermal [1] and mechanical [2] sensors to high-power [3] and electronic [4,5] nanodevices, owing to its superior characteristics including high breakdown voltage, high intrinsic thermal conductivity and wide band gap. Among many polytypes, two hexagonal (4H–SiC and 6H–SiC) and one cubic (3C–SiC) phases are the most frequently studied and used. 3C–SiC, with a simple zinc blende structure, can grow with high crystal quality on silicon and 4H–SiC substrates [6–9]. Heavily doped (10^{18}–10^{21} cm^{-3}) samples of this semiconductor are required for some applications [10–12]. In particular, highly B-doped and N-doped 3C–SiC can be applied in single-junction solar cells [13,14] and optoelectric devices [15,16], respectively.

Progress has been made recently in the fundamental understanding of the themal conductivity reduction in doped 3C–SiC. On the one hand, Protik et al. [17] have found that both phonon-electron scattering and phonon-defect scattering owing to mass disorder lead to negligible κ reduction around room temperature in lightly doped 2H-, 4H- and 6H–SiC. For 3C–SiC, Wang et al. have demonstrated that phonon-electron scattering can be comparable to anharmonic scattering in both the electron- and hole-doped cases [18]. It is however unclear to what degree phonon-electron scattering affects the thermal conductivity when the defect scattering of phonons is also taken into account. Dongre et al. [19] showed that in highly doped Si a good agreement with experimental results could be obtained only when considering both phonon-electron and phonon-defect scattering. However, in boron-doped 3C–SiC, phonon-defect scattering is substantially stronger due to a resonance in the scattering rates [20]. Although this would seem to suggest the importance of describing both phonon-defect and phonon-electron scattering in 3C–SiC, a combined study of both types of scattering is lacking.

In this work, we have calculated the κ of heavily N-doped and B-doped 3C–SiC taking into account both phonon-electron (ph-el) and phonon-defect (ph-def) scattering from first principles. We observe that in the N-doped case, both scattering mechanisms can effectively contribute to the κ reduction. Specifically, ph-el scattering governs the κ reduction at defect concentrations lower than ~10^{20} cm^{-3} at ambient temperature. Above this doping level, however, it is ph-def scattering that becomes dominant. On the other hand, ph-def scattering exclusively

* Corresponding author. Institute for Advanced Study, Shenzhen University, Shenzhen, 518060, China
E-mail address: wu.li.phys2011@gmail.com (W. Li).

https://doi.org/10.1016/j.mtphys.2024.101346
Received 5 October 2023; Received in revised form 24 January 2024; Accepted 25 January 2024
Available online 3 February 2024

dominates the reduction of κ over the whole temperature and doping ranges studied in the B-doped case. Moreover, we also take 4H–SiC as a case study of a hexagonal polytype and observe similar features.

2. Methodology

Within the framework of the phonon Boltzmann transport equation (BTE), the lattice thermal conductivity tensor can be calculated as [21,22]:

$$\kappa = \frac{1}{k_B T^2 \Omega Z} \sum_{\lambda} n_{\lambda}^0 (n_{\lambda}^0 + 1)(\hbar\omega_{\lambda})^2 \boldsymbol{v}_{\lambda} \otimes \boldsymbol{F}_{\lambda}, \tag{1}$$

where Ω denotes the volume of the unit cell and Z is the total number of $\mathbf{q}$ points on a regular grid sampling the Brillouin Zone. λ describes a phonon mode with branch index s and wave vector $\boldsymbol{q}$. n_{λ}^0, ω_{λ} and $\boldsymbol{v}_{\lambda}$ correspond to the Bose-Einstein occupancy, the angular frequency and the group velocity of phonon mode λ, respectively. $\boldsymbol{F}_{\lambda}$ can be interpreted as a phonon mean free displacement or as a vector characterizing the deviation from equilibrium of the phonon populations in the linear regime. Hence the linearized BTE can be expressed as:

$$\boldsymbol{F}_{\lambda} = \tau_{\lambda}(\boldsymbol{v}_{\lambda} + \Delta_{\lambda}). \tag{2}$$

Here, Δ_{λ} is a linear combination of $\boldsymbol{F}_{\lambda}$ vectors, as described in Ref. [21]. Therefore, in practice, Eq. (2) can be solved accurately with an iteration scheme starting from the relaxation-time approximation of neglecting the Δ_{λ} term. τ_{λ} denotes the phonon relaxation time, whose inverse is the scattering rate, which comprises the contributions from three-phonon processes $(1/\tau_{\lambda}^{3\mathrm{ph}})$, isotopic mass disorder $(1/\tau_{\lambda}^{\mathrm{iso}})$, ph-el scattering $(1/\tau_{\lambda}^{\mathrm{ph-el}})$ and ph-def scattering $(1/\tau_{\lambda}^{\mathrm{ph-def}})$ in doped semiconductors, as expressed by the Matthiessen rule:

$$\frac{1}{\tau_{\lambda}} = \frac{1}{\tau_{\lambda}^{3\mathrm{ph}}} + \frac{1}{\tau_{\lambda}^{\mathrm{iso}}} + \frac{1}{\tau_{\lambda}^{\mathrm{ph-el}}} + \frac{1}{\tau_{\lambda}^{\mathrm{ph-def}}} \tag{3}$$

Three-phonon scattering rates, including the absorption and emission processes allowed under the conservation of energy and momentum, dominate the intrinsic thermal conductivity around room temperature. They can be obtained from density functional theory and density functional perturbation theory. The effect of isotopic mass disorder reflects the natural isotopic distributions of the elements involved. The detailed expressions of the above two scattering rates are included in Ref. [21].

2.1. Phonon-electron scattering

In the last two decades, the predictive calculation of electron-phonon interaction (EPI) has become feasible using first-principles approaches. The ph-el scattering rates, directly related to the coupling matrix elements of EPI, can be calculated as [23–25]:

$$\frac{1}{\tau_{\lambda}^{\mathrm{ph-el}}} = 2\frac{2\pi}{\hbar} \sum_{mn,\boldsymbol{k}} \left|\boldsymbol{\varphi}_{mn}^{i}(\boldsymbol{k},\boldsymbol{q})\right|^2 (f_{n\boldsymbol{k}} - f_{m\boldsymbol{k}+\boldsymbol{q}}) \delta(\epsilon), \tag{4}$$

where $\delta(\varepsilon)$, with $\varepsilon = \mathrm{E}_{\mathbf{mk}+\mathbf{q}} - \mathrm{E}_{\mathbf{nk}} - \hbar\omega_{\lambda}$, is the Dirac delta function arising from the energy conservation. $f_{n\boldsymbol{k}}$ is the Fermi-Dirac distribution for electrons in the equilibrium state and $E_{n\boldsymbol{k}}$ denotes the eigenenergy of an electron in a state $\{n\boldsymbol{k}\}$. The factor of 2 appearing before the summation accounts for the spin degeneracy. $\boldsymbol{\varphi}_{mn}^{i}(\boldsymbol{k},\boldsymbol{q})$ is the screened coupling matrix element of a ph-el scattering process in which a phonon from mode λ and two charge carriers with band indices m and n and wave vectors $\boldsymbol{k}$ and $\boldsymbol{k}+\boldsymbol{q}$, respectively, participate. Strictly speaking, the product $|\boldsymbol{\varphi}|^2$ is an approximation to $\boldsymbol{\varphi}^b\boldsymbol{\varphi}^*$ where the bare matrix $\boldsymbol{\varphi}^b$ is replaced by the screened $\boldsymbol{\varphi}$ [25]. Very recently it has been shown that this doubly screened approximation is very reliable due to its designed error cancellation to first order [26,27]. Although using one bare $\boldsymbol{\varphi}^b$ [28] could in principle improve the results, it is challenging in practice and relies on the achievable precision of the screened $\boldsymbol{\varphi}$. Furthermore, another neglected screening effect due to the presence of doping-induced free carriers can reduce the Fröhlich coupling, which overestimates the LO phonon contribution to electron scattering rates [29]. On the other hand, the LO phonon scattering rates due to electrons could also be affected. However, this effect on thermal transport should be small since LO phonons barely contributed to κ.

We also point out that electrons are taken to be in equilibrium when calculating ph-el scattering rates, which thus leads to the decoupled BTE. More rigorously, those interactions between non-equilibrium electrons and phonons should also be considered within the coupled el-ph BTEs [30]. Recent studies have found that it has significant effects on Seebeck coefficient and mobility in doped semiconductors [31]. However, the effect on κ is overall weak as demonstrated in Refs. [32,33].

Note that ph-el scattering, even though negligible in intrinsic semiconductors, can lead to a non-negligible κ reduction in highly doped semiconductors and metals due to a larger number of free carriers [34]. However, in contrast to metals, the ph-el scattering in highly doped semiconductors is strongly temperature-dependent [19].

2.2. Phonon-defect scattering

In the context of the atomistic Green's function formalism for describing the defect-induced phonon transition rate, the ph-def scattering can be calculated using the optical theorem [20,35]:

$$\frac{1}{\tau_{\lambda}^{\mathrm{ph-def}}} = -C_{\mathrm{def}} \frac{\Omega}{\omega_{\lambda}} \mathrm{Im}\{\langle\lambda|\mathbf{T}|\lambda\rangle\}, \tag{5}$$

where C_{def} denotes the volume concentration of defects. $\boldsymbol{T}$, the matrix bridging the Green's function between perturbed and unperturbed systems, can be built as:

$$\boldsymbol{T} = [\boldsymbol{I} - \boldsymbol{V}\boldsymbol{g}^{+}]^{-1}\boldsymbol{V}, \tag{6}$$

where $\boldsymbol{I}$ is the identity matrix and $\boldsymbol{g}^{+}$ is the retarded Green's function for the system without defects. The detailed calculation of $\boldsymbol{g}^{+}$can be found in Ref. [36]; $\boldsymbol{V}$ is the perturbation describing the changes introduced in the dynamical equations by the introduction of a defect and can be rewritten as [20].

$$\boldsymbol{V} = \boldsymbol{V}_M + \boldsymbol{V}_K, \tag{7}$$

where $\boldsymbol{V}_M$ and $\boldsymbol{V}_K$ are the mass and interatomic force constants (IFCs) perturbation matrices between the host and defect-laden systems, respectively. Here, $\boldsymbol{V}_M$ is a diagonal matrix, whose only nonzero elements are the onsite terms of defects, with values:

$$\boldsymbol{V}_M^{i\alpha,j\beta} = -\frac{M_i^{'} - M_j}{M_i} \omega_{\lambda}^2 \delta_{ij} \delta_{\alpha\beta}, \tag{8}$$

where i and j are atomic site indices, α and β identify Cartesian axes, and M_i and $M_i^{'}$ denote the masses of the host atom and the defect atom replacing it at the i-th site. On the other hand, $\boldsymbol{V}_K$ characterizes the systematic IFCs changes, the matrix elements of which are expressed as:

$$\boldsymbol{V}_K^{i\alpha,j\beta} = \frac{K_{i\alpha,j\beta}^{'} - K_{i\alpha,j\beta}}{\sqrt{M_i M_j}}. \tag{9}$$

here, $K_{i\alpha,j\beta}^{'}$ and $K_{i\alpha,j\beta}$ are the second derivatives of the potential energy of the defect-laden and perfect systems, respectively, evaluated at equilibrium.

Since defects can exist in different charge states (q) in the doped system, the total defect concentration $C_{\mathrm{def}} = \sum_q C_{X^q}$, where C_{X^q} is the concentration of specific defect X in charge state q. Correspondingly, the

total ph-def scattering rate due to a specific type of defects can be expanded as [37]:

$$\frac{1}{\tau_{\lambda}^{\mathrm{ph-def}}} = -\sum_{q} C_{X^q} \frac{\Omega}{\omega_{\lambda}} \mathrm{Im}\{\langle\lambda|\mathbf{T_q}|\lambda\rangle\}. \tag{10}$$

2.3. Calculations of carrier concentrations

In the doped system, ph-el scattering rates, similar to ph-def scattering, are related to carrier concentrations. The electron and hole concentrations (n and p) are determined by the Fermi level μ. Considering a system with given donor and acceptor concentrations (C_D and C_A), the charge neutrality condition, determining μ, is expressed as [37,38]:

$$n + C_A^- = p + C_D^+, \tag{11}$$

with

$$C_A^- = \frac{C_A}{1 + g_A \cdot \exp[(E_A - \mu)/k_B T]} \tag{12}$$

and

$$C_D^+ = \frac{C_D}{1 + g_D \cdot \exp[(\mu - E_D)/k_B T]}, \tag{13}$$

where C_A^- (C_D^+) represents the concentration of ionized acceptors (donors), and E_A(E_D) and g_A(g_D) are the energy level and spin degeneracy factor of acceptors (donors), respectively. g_D and g_A take the values 2 and 6 in our calculations due to the triply degenerate valence band in 3C–SiC.

Within the parabolic band approximation, the density of states (DOS) depends on the DOS effective mass m_e^* and m_h^* for the conduction and valence bands, respectively. Consequently,

$$n = \frac{2(2\pi m_e^* k_B T)^{3/2}}{h^3} \frac{2}{\sqrt{\pi}} F_{1/2}\left(\frac{\mu - E_c}{k_B T}\right), \tag{14}$$

and

$$p = \frac{2(2\pi m_h^* k_B T)^{3/2}}{h^3} \frac{2}{\sqrt{\pi}} F_{1/2}\left(\frac{E_v - \mu}{k_B T}\right), \tag{15}$$

where E_c and E_v represent the energy of the conduction and valence band edges, respectively. The Fermi-Dirac integral $F_{1/2}$ is defined as

$$F_{1/2}(x) = \int_0^{\infty} \frac{\epsilon^{1/2}}{e^{\epsilon - x} + 1} d\epsilon. \tag{16}$$

The parameters involved in the calculation are taken from experiments. m_e^* and m_h^* are taken as $0.72m_0$ and $0.6m_0$ with free electron mass m_0 respectively [39,40]. The band gap ($E_c - E_v$) is 2.416 eV, and considered independent of the doping and temperature [41]. In principle, the ionized defect concentrations (C_{X^q}) and free carrier concentrations in terms of μ at specific T, can be obtained by solving Eq. (11) self-consistently [37,42].

In this work we examine two prevalent substitutional defects of N (donor) and B (acceptor) atoms in 3C–SiC, which can in principle occupy Si sites (N_{Si} and B_{Si}) and C sites (N_C and B_C). Here we assume that these defects are introduced into 3C–SiC in Si-rich conditions at high growth temperature (T_g) [43] and the quenching process leaves C_{def} unchanged, but the ratio of neutral and ionized defects changes at lower temperatures [37,44]. In the N-doped case with a total concentration $C_{\mathrm{def}} = C_D(N_C) + C_D(N_{Si})$, the ratio of these Si-site and C-site defect concentrations is related to the defect formation energy (DFE) of defect thermodynamics through a factor $\exp[-[E_f(N_{Si}) - E_f(N_C)]/(k_B T_g)]$, where $E_f(N_{Si})$ and $E_f(N_C)$ are DFEs of N_{Si} and N_C respectively. This also applies to the B-doped case. Previous calculations have found that in Si-rich conditions the DFEs are larger for N_{Si} and B_{Si} than for N_C and B_C defects, with differences of ~5 eV and 1 eV [45–48], respectively. These cause the above factor almost zero in both cases, which suggests negligible numbers of Si-site defects and $C_{\mathrm{def}} \approx C_D(N_C)$ or $C_A(B_C)$ in the doped systems.

After doping the defects can be partially ionized at a finite temperature. While ionization energy can be derived from the crossing points of DFE lines, here we adopt the ionization energy of N_C and B_C defects determined from experiments, corresponding to ($E_c - E_D$) and ($E_A - E_v$), as 0.055 eV and 0.735 eV [43], respectively.

The experimental 3C–SiC samples grown under Si-rich conditions usually include intrinsic defects. They may compensate the extrinsic defect doping according to a Boltzmann distribution of $N_\alpha g_\alpha \exp[-E_f(\alpha)/(k_B T)]$, where N_α, g_α and $E_f(\alpha)$ are the occupied sites number, degeneracy factor and DFE of defect α [38]. Previous studies found that carbon vacancies and silicon antisites are predominant, with lower DFEs as compared to any other intrinsic defects [49–54]. However, the DFE values of these two defects are still higher than those of N_C and B_C. Therefore, the compensation effects caused by them should be negligible within the doping and temperature ranges considered in our calculations.

3. Computation details

We carried out the structural optimization of the perfect 3C–SiC crystals using the VASP density functional theory (DFT) package [55], with the projector-augmented-wave method and local density approximation (LDA) to the exchange and correlation functional. The calculated band gap of perfect system is 1.34 eV (Fig. S1) [56], smaller than the experimental value of 2.416 eV [57], which arises from the delocalization error of LDA functional [58,59]. However, the band gap has little effect on the calculated thermal transport properties since the transitions across the gap do not contribute in our calculated electronic structure. Next, the Phonopy package [60] was used to calculate the harmonic IFCs of perfect structures with 5 × 5 × 5 supercells and Γ-sampling. Phonon dispersion agrees better with experimental results [61,62] than the one calculated from the generalized gradient approximation (GGA) functional [63], as shown in Fig. S1 [56]. For the anharmonic third-order IFCs, the thirdorder.py code in ShengBTE package [21] was used, also with a 5 × 5 × 5 supercell and Γ-sampling, as well as a cutoff of 5 Å in the interaction range.

The ph-def scattering rate calculations for neutral and ionized defects were executed using the almaBTE code [64] with the same parameters as in Refs. [20,65]. We first employed 5 × 5 × 5 supercell with one specific defect replacing the carbon site to perform structural relaxation. The Phonopy package was then used to extract harmonic IFCs of this defective supercell. The harmonic IFCs matrices of perfect and defective supercells, which correspond to the K and K' terms in Eq. (9) respectively, were used to measure the bonding perturbation. The Green's functions of the perfect system were calculated on a 18 × 18 × 18 grid using the tetrahedron method to integrate over the Brillouin-zone and the ph-def scattering rates were then calculated with a coarse 20 × 20 × 20 $\boldsymbol{q}$-grid. To achieve denser $\boldsymbol{q}$-grid and reduce computation cost, a linear interpolation method was used to interpolate the entire ph-def scattering rates onto the 40 × 40 × 40 $\boldsymbol{q}$-grid. As bonding perturbation is localized around the defect, we also calculated ph-def scattering rates using a 4 × 4 × 4 supercell (in Fig. S2) [56] and found that the 5 × 5 × 5 supercell yielded almost converged rates in each doped case.

With regard to the calculation of ph-el scattering rates, electron-phonon coupling matrix elements $\boldsymbol{\varphi}_{mn}^{i}(\boldsymbol{k}, \boldsymbol{q})$ in Eq. (4) were first calculated on coarse 6 × 6 × 6 $\boldsymbol{k}$- and $\boldsymbol{q}$-grids with the Quantum Espresso DFT package [66]. We then interpolated them onto denser 80 × 80 × 80 $\boldsymbol{k}$-grid and 40 × 40 × 40 $\boldsymbol{q}$-grid, respectively, through the Wannier function interpolation method as implemented in the EPW package [67].

After ph-def and ph-el scattering were determined, the exploration of bulk κ is straightforward. This was implemented in a modified version of the ShengBTE package [21] using a 40 × 40 × 40 $\boldsymbol{q}$-grid to ensure convergence of κ. In this case, the following phonon scattering mechanisms were taken into account: anharmonic scattering, isotopic disorder, ph-def and ph-el scattering.

4. Results and discussion

The temperature dependence of carrier concentration n_c for several defect concentrations in N- and B-doped 3C–SiC is shown in Fig. 1. In the N-doped case with a defect concentration of 10^{17} cm^{-3}, a clear plateau with $n_c = C_{\text{def}}$ emerges between 200 and 1600 K. At higher C_{def}, although the temperature dependence of n_c remains weak at intermediate temperatures, n_c is smaller than C_{def}, indicating that the doping becomes less effective in contributing to the carriers. Owing to the more than one order of magnitude higher ionization energy for B defects than for N defects, the holes supplied by B defects cannot be effectively excited. As a result, n_c for the B-doped case is much smaller than the corresponding value in the N-doped case with the same C_{def} except at high temperatures. For instance, at 300 K, for doping of 10^{19} and 10^{21} cm^{-3}, $n_c = 2.5 \times 10^{18}$ and 2.3×10^{19} cm^{-3} in the N_C case, whereas $n_c = 3.0 \times 10^{12}$ and 3.0×10^{13} cm^{-3} in the B_C case. At high temperatures, the doping has a lesser effect on carrier concentration. When the doping effect is completely eliminated, the intrinsic region, in which $n = p$, is recovered. This happens above 1800 K at $C_{\text{def}} = 10^{17}$ cm^{-3}.

The intrinsic anharmonic, extrinsic ph-def and ph-el scattering rates at room temperature are plotted in Fig. 2 and Fig. 3 for N- and B-doped cases. Since the ph-def scattering rates are proportional to the defect concentration, only those for doping of 10^{21} cm^{-3} are shown. Although ph-el scattering rates do not have a simple dependence on C_{def}, they increase with concentration in a markedly less than linear way [19]. In fact, in the intrinsic region, ph-el scattering rates are independent of C_{def}. In Figs. 2 and 3, only the results of $C_{\text{def}} = 10^{19}$ and 10^{21} cm^{-3} are shown.

In both cases, ph-def scattering by ionized defects is generally weaker than that by neutral defects. This can be ascribed to the electronic structure of the ionized defect system more closely resembling that of host system, which causes a smaller bonding perturbation term in Eq. (6) [37,65]. At low frequencies (below 30 rad/ps) the ph-def scattering rates exhibit a classical Rayleigh behavior($\propto \omega^4$). In contrast, the ph-el scattering rates have a much weaker ω dependence, especially in the B-doped case.

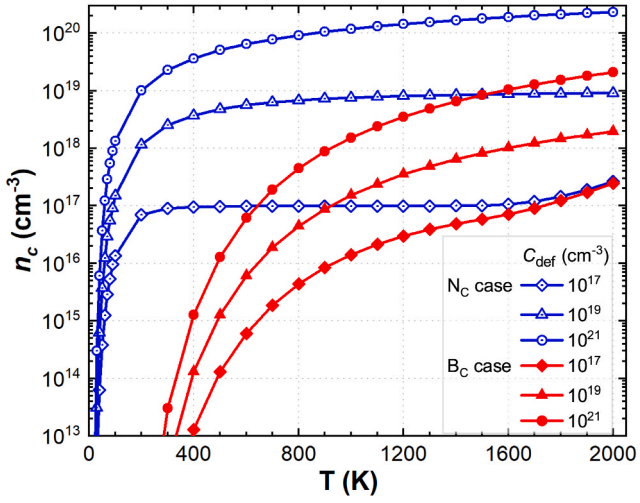

Fig. 1. The temperature dependent carrier concentrations n_c of N-doped and B-doped 3C–SiC with defect concentrations C_{def} of 10^{17}, 10^{19} and 10^{21} cm^{-3}. The calculations only consider N_C (blue lines) and B_C (red lines) substitutions for these doped cases, respectively.

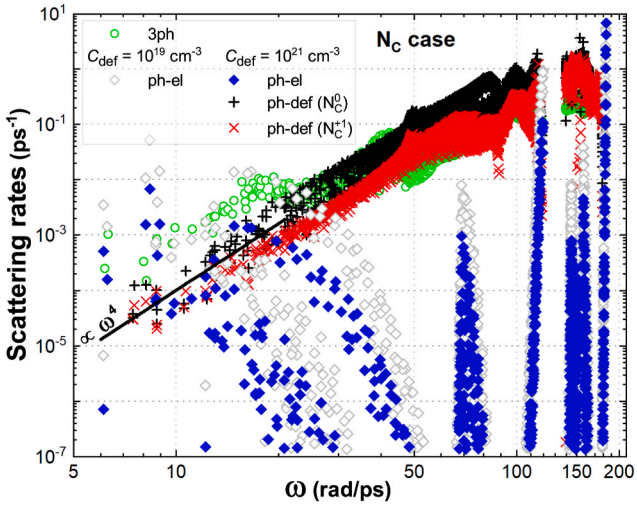

Fig. 2. Comparison among scattering rates from three-phonon (3ph) scattering, ph-def scattering by the neutral (N_C^0) and ionized defects (N_C^{+1}) with C_{def} of 10^{21} cm^{-3}, and ph-el scattering with C_{def} of 10^{19} and 10^{21} cm^{-3} at 300 K in N-doped 3C–SiC.

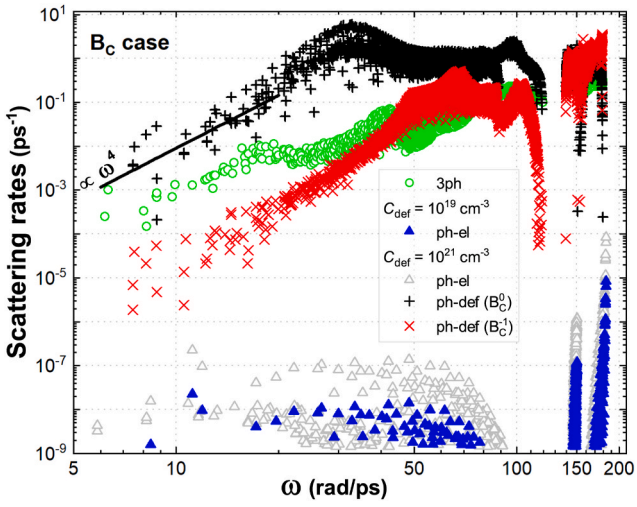

Fig. 3. Comparison among scattering rates from three-phonon (3ph) scattering, ph-def scattering by the neutral (B_C^0) and ionized defects (B_C^{-1}), and ph-el scattering with C_{def} of 10^{19} and 10^{21} cm^{-3} at 300 K in B-doped 3C–SiC.

In the N-doped case, both the ph-def and ph-el scattering rates are comparable to the anharmonic scattering, while the ph-el scattering is stronger than the ph-def scattering at low frequencies.

In the B-doped case, the ph-def scattering by neutral defects can be even orders of magnitude stronger than that by ionized defects and the anharmonic scattering. It has been shown that this unusually strong phonon scattering of neutral B defects is a result of a strong perturbation of the IFCs, Eq. (9), caused by the proximity of multiple minima in the potential energy surface [65]. It directly leads to the resonant scattering behavior present at low frequencies [68]. In contrast, ph-el scattering is negligible over the whole frequency range when compared to anharmonic and ph-def scattering. This is mainly due to the low carrier concentrations caused by the high ionization energy of B defects. In fact, for the same value of n_c, ph-el scattering due to holes is even stronger than that due to electrons [18].

The extrinsic ph-def and ph-el scattering can lead to reduction in the intrinsic κ. Figs. 4 and 5 show the reduction in the spectral contributions

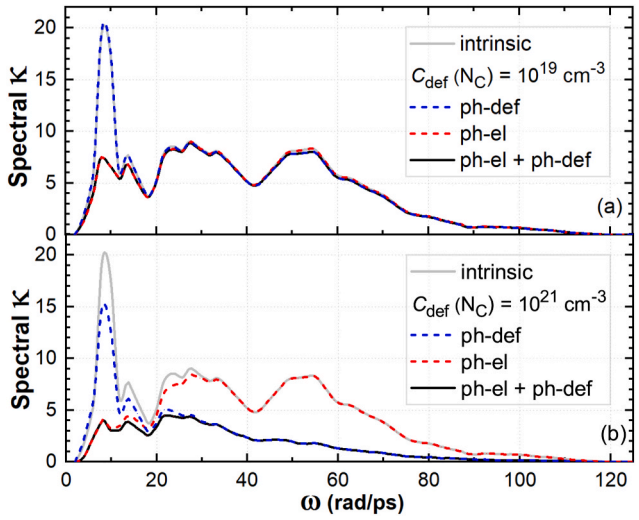

Fig. 4. Spectral contributions to κ at 300 K for the intrinsic and N-doped cases with defect concentrations of (a) 10^{19} cm^{-3} and (b) 10^{21} cm^{-3}. Note that both the intrinsic and extrinsic cases include anharmonic and isotope effects on κ, while the latter also includes ph-el and ph-def scattering individually and together.

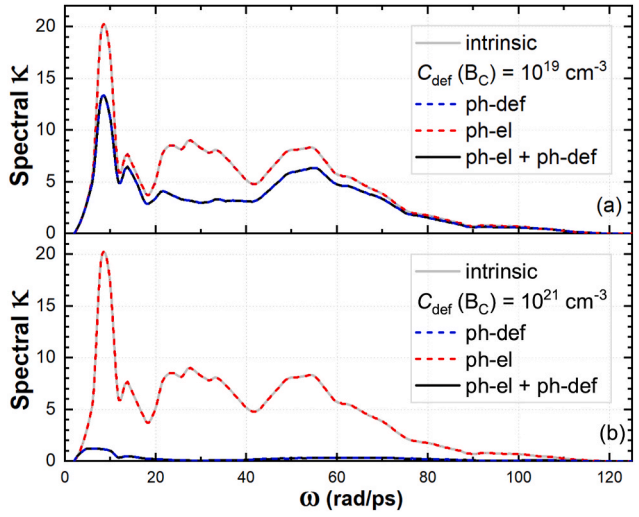

Fig. 5. Spectral contributions to κ at 300 K for the intrinsic and B-doped cases with defect concentrations of (a) 10^{19} cm^{-3} and (b) 10^{21} cm^{-3}. Note that both the intrinsic and extrinsic cases include anharmonic and isotope effects on κ, while the latter also includes ph-el and ph-def scattering individually and together.

to κ at 300 K due to these two extrinsic scattering individually and combined for the N- and B-doped 3C–SiC, respectively. According to Eq. (10), the total ph-def scattering rates are contributed from both neutral and ionized defects, weighted by their respective concentration. However, the ionized defect contribution to ph-def scattering in the B-doped case is completely neglected due to its much lower concentrations and ph-def scattering rates.

The intrinsic κ, only taking anharmonic and isotope scattering into account, is contributed mostly by low-frequency phonons up to 115 rad/ps. Due to the distinct scattering rate characteristics, the effects of doping with B or N defects are very different. B defects affect κ mostly by ph-def scattering, whereas N defects can reduce κ effectively by both ph-el and ph-def scattering. This is evident in Fig. 2 when looking at scattering rates below 18 rad/ps.

More specifically, for N doping at $C_{def} = 10^{19}$ cm^{-3}, ph-el scattering causes κ to decrease at low frequencies up to 18 rad/ps, while ph-def scattering is too weak to affect κ over the whole frequency range. As C_{def} increases to 10^{21} cm^{-3}, the ph-def scattering becomes effective in reducing κ, especially above 18 rad/ps. Although ph-def scattering also affects the lower frequency contributions, they remain dominated by ph-el scattering. Therefore, the κ reductions due to these two extrinsic scattering are almost additive.

On the other hand, owing the nature of the neutral B defect as an exceptionally strong phonon scatterer, κ can be reduced significantly. At B doping of 10^{19} cm^{-3}, all but the contributions from the very low and high frequency phonons are affected. At $C_{def} = 10^{21}$ cm^{-3}, κ almost vanishes, and only has little contribution from the low-frequency phonons left. Since ph-el scattering is extremely weak, its effect on κ can be simply neglected.

Fig. 6 shows the κ reduction at 300 K as a function of C_{def} in the N- and B-doped cases. Considering both ph-el and ph-def scattering, κ in the N_C case starts decreasing at 10^{16} cm^{-3}, one order of magnitude lower than the threshold C_{def} in the B_C case. However, the latter case can cause much faster κ decrease. In particular, when C_{def} is 10^{18}, 10^{19} and 10^{20} cm^{-3}, κ is reduced by 8 %, 12 % and 30 % in the N_C case and reduced by 7 %, 33 % and 73 % in the B_C case, respectively.

This extrinsic scattering in the N_C case dominates the κ reduction at various C_{def} ranges. Below 10^{19} cm^{-3}, the κ reduction is entirely due to the ph-el scattering. With a stronger dependence on C_{def}, ph-def scattering plays an increasingly important role in the reduction as C_{def} increases. In particular, at around 10^{20} cm^{-3}, the ph-def scattering is comparable to the ph-el scattering, and both lead to 15 % reduction in κ. Above this level, the κ decrease becomes dominated by the ph-def scattering.

In contrast, the reduction in the B_C case is entirely attributed to the ph-def scattering, due to the exceptionally strong ph-def scattering and weak ph-el scattering. Our calculated values can agree well with the measured one [9]. Note again that ph-el scattering alone leads to a weaker reduction in κ in the B_C case than in the N_C case with the same C_{def}, although the opposite is true when considering the same n_c [18]. Those B defects are lying deep in the band gap and more stable in the neutral state [65]. Therefore, it is difficult to achieve an n_c as high as 10^{21} cm^{-3} at room temperature by B doping.

Next we turn to study the temperature dependence of κ for two representative defect concentrations $C_{def} = 10^{19}$ and 10^{20} cm^{-3}. The results are plotted in Fig. 7. In the N-doped case with 10^{19} cm^{-3}, ph-def scattering contributes negligibly to κ reduction, particularly above room

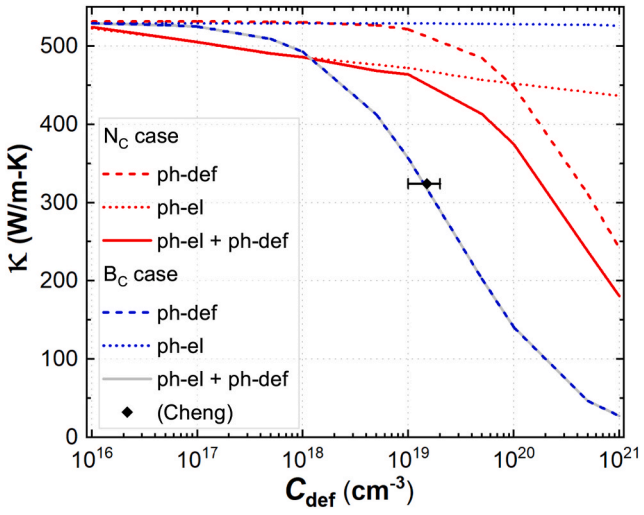

Fig. 6. Comparison of the κ reduction at 300 K for extrinsic N- and B-doped cases due to ph-el and ph-def scattering individually and together at various defect concentration from 10^{16} to 10^{21} cm^{-3}. The measured data is taken from ref. [9].

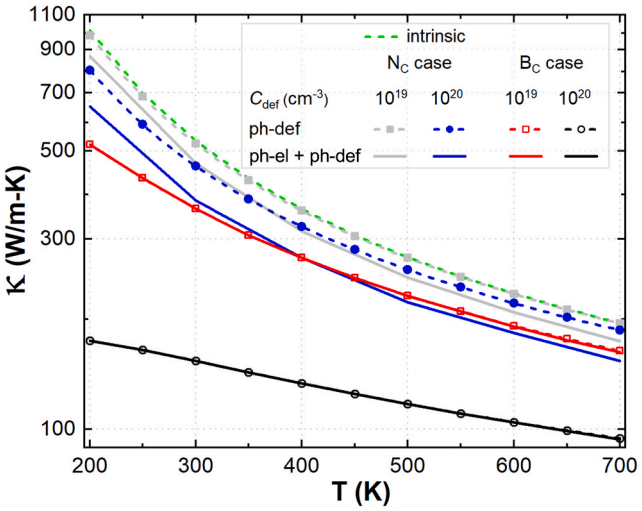

Fig. 7. Temperature dependence (200–700 K) of κ for the N- and B-doped cases with defect concentrations of 10^{19} and 10^{20} cm^{-3}. These cases include ph-def and ph-el scattering individually and together.

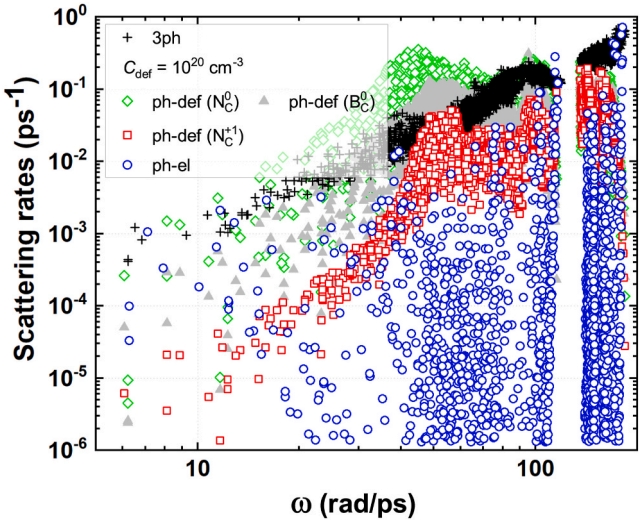

Fig. 8. Phonon-defect (ph-def) scattering rates of neutralB_C^0, neutral N_C^0 and charged N_C^{+1} defects at defect concentration (C_{def}) of 10^{20} cm^{-3}, together with the corresponding phonon-electron (ph-el) scattering rates with electron concentration of 7×10^{18} cm^{-3} and three-phonon (3ph) scattering rates at 300 K in 4H–SiC.

temperature, indicating that considering ph-el scattering alone can reproduce the κ reduction over the entire temperature range. When that doping level is increased up to 10^{20} cm^{-3}, ph-def scattering becomes important for decreasing κ, with an effect comparable to the ph-el scattering below 300 K. In the B_C case, the ph-el scattering remains negligible over the whole temperature range at these two defect concentrations.

It is interesting to note that B_C at a concentration of 10^{19} cm^{-3} leads to the same amount of reduction in κ as the N_C case at 10^{20} cm^{-3} does around 400 K. As the ph-def scattering is T-independent and the intrinsic anharmonic scattering increases linearly with T, the relative κ suppression becomes weaker at higher temperatures. This is evident in the B_C case. Considering that the ph-el scattering increasing with T plays a role in the N_C case, the κ decreases faster than in B_C case, thus leading to a smaller κ above 400 K in the N_C case with a concentration of 10^{20} cm^{-3}.

We expect that the findings for cubic SiC can be applied to other polytypes with lower defect ionization energies, since ph-el scattering rates are positively correlated with carrier concentrations and unusually strong ph-def scattering only appears in very particular circumstances [65]. We now present a case study of hexagonal phase 4H–SiC [69,70]. We compare the rates of intrinsic three-phonon, ph-el and ph-def scattering with $C_{def} = 10^{20}$ cm^{-3} at room temperature in Fig. 8. In the B-doped case, The ionization energy of B defects (~0.65 eV) [71] is much larger, which leads to weak ph-el scattering rates that can be naturally excluded due to the very small carrier concentrations. Therefore, we only need to consider ph-def scattering of neutral defects, whose rates are comparable to three-phonon scattering rates. In contrast, the N defect ionization energy is lower (~0.07 eV) [71] and we evaluated both ph-el and ph-def scattering rates in this case. In the low frequency range where phonons contribute the most to κ, the rates of ph-el scattering and ph-def scattering from neutral defects are comparable to those from three-phonon processes. Therefore, one can expect that ph-el and ph-def scattering should also be significant for κ reduction of highly N-doped 4H–SiC, in contrast to the B-doped case.

5. Conclusion

From first principles calculations, the κ of highly N- and B-doped 3C–SiC has been studied by combining the extrinsic ph-def and ph-el scattering along with the intrinsic anharmonic and isotope scattering. In the N-doped case, at low N concentrations below 10^{19} cm^{-3}, the κ reduction is attributed to low frequency phonons, which are affected by ph-el scattering exclusively. For the higher N defect concentrations, the reduced contribution from the high frequency phonons caused by the ph-def scattering primarily account for the κ reduction. Even so, the κ reduction can be accurately obtained only when both scattering are considered at high defect concentrations. In the case of B doping, the κ reduction can be attributed to the ph-def scattering alone over the entire concentration range, due to stronger ph-def scattering and weaker ph-el scattering as compared to the N doped case. As was revealed previously, the stronger phonon scattering by neutral B defects results from the proximity of several minima in the potential energy surface. The much larger ionization energy of B acceptors than N donors results in much weaker ph-el scattering in B-doped 3C–SiC with the same defect concentration, though the ph-el scattering are much stronger in the B-doped than in the N-doped case with the same carrier concentration n_c. We expect that the similar features can be found in other polytypes with low defect ionization energies.

CRediT authorship contribution statement

Guijian Pang: Writing – review & editing, Writing – original draft, Software, Methodology, Investigation, Formal analysis, Data curation, Conceptualization. **Fanchen Meng:** Writing – review & editing, Methodology, Investigation, Data curation. **Yani Chen:** Writing – review & editing, Methodology, Investigation, Formal analysis. **Ankita Katre:** Writing – review & editing, Software, Formal analysis, Data curation. **Jesús Carrete:** Writing – review & editing, Software, Investigation, Formal analysis. **Bonny Dongre:** Writing – review & editing, Software, Formal analysis, Data curation. **Georg K.H. Madsen:** Writing – review & editing, Investigation, Funding acquisition, Formal analysis. **Natalio Mingo:** Writing – review & editing, Investigation, Formal analysis. **Wu Li:** Writing – review & editing, Software, Methodology, Funding acquisition, Conceptualization.

Declaration of competing interest

The authors declare that they have no known competing financial interests or personal relationships that could have appeared to influence the work reported in this paper.

Data availability

The authors are unable or have chosen not to specify which data has been used.

Acknowledgments

We acknowledge support from the Natural Science Foundation of China (NSFC) (Grants No. 12174261 and No. 12104312), the Guang-Dong Basic and Applied Basic Research Foundation (Grants No. 2023A1515010365 and No. 2022A1515011877) and the Austrian Science Funds (FWF) for funding under project CODIS (Grant No. FWF-I-3576-N36).

References

[1] V. Balakrishnan, T. Dinh, H.P. Phan, D.V. Dao, N.T. Nguyen, Sens. Actuators Phys. 279 (2018) 293.
[2] H.P. Phan, D.V. Dao, K. Nakamura, S. Dimitrijev, N. Nguyen, J. Microelectromech. Syst. 24 (2015) 1663.
[3] M. Bhatnagar, B.J. Baliga, IEEE Trans. Electron. Dev. 40 (1993) 645.
[4] A. Itoh, H. Matsunami, Crit. Rev. Solid State Mater. Sci. 22 (1997) 111.
[5] N.G. Wright, A.B. Horsfall, K. Vassilevski, Mater. Today 11 (2008) 16.
[6] S. Nishino, J.A. Powell, H.A. Will, Appl. Phys. Lett. 42 (1983) 460.
[7] P. Tanner, L. Wang, S. Dimitrijev, J. Han, A. Iacopi, L. Hold, G. Walker, Sci. Adv. Mater. 6 (2014) 1542.
[8] V. Jokubavicius, G.R. Yazdi, R. Liljedahl, I.G. Ivanov, R. Yakimova, M. Syväjärvi, Cryst. Growth Des. 14 (2014) 6514.
[9] Z. Cheng, J. Liang, K. Kawamura, H. Zhou, H. Asamura, H. Uratani, J. Tiwari, S. Graham, Y. Ohno, Y. Nagai, et al., Nat. Commun. 13 (2022) 7201.
[10] R.A. Abram, G.J. Rees, B.L.H. Wilson, Adv. Phys. 27 (1978) 799.
[11] M. Spera, G. Greco, R.L. Nigro, C. Bongiorno, F. Giannazzo, M. Zielinski, F. La Via, F. Roccaforte, Mater. Sci. Semicond. Process. 93 (2019) 295.
[12] G.S. Sun, J. Ning, X.F. Liu, Y.M. Zhao, J.Y. Li, L. Wang, W.S. Zhao, L. Wang, in: textitMater. Sci. Forum, vol. 556, Trans Tech Publ, 2007, pp. 179–182.
[13] J.W. Sun, V. Jokubavicius, L. Gao, I. Booker, M. Jansson, X.Y. Liu, J.P. Hofmann, E. J. Hensen, M.K. Linnarsson, P.J. Wellmann, et al., in: textitMater. Sci. Forum, vol. 858, Trans Tech Publ, 2016, pp. 1028–1031.
[14] M. Syväjärvi, Q. Ma, V. Jokubavicius, A. Galeckas, J. Sun, X. Liu, M. Jansson, P. Wellmann, M. Linnarsson, P. Runde, et al., Sol. Energy Mater. Sol. Cells 145 (2016) 104.
[15] J. Wang, X. Fang, G. Feng, W. Song, Z. Hou, H. Jin, J. Yuan, M. Cao, Phys. Lett. A 374 (2010) 2286.
[16] S. Yoshida, K. Endo, E. Sakuma, S. Misawa, H. Okumura, H. Daimon, E. Muneyama, M. Yamanaka, MRS Online Proc. Libr. 97 (1987) 259.
[17] N.H. Protik, A. Katre, L. Lindsay, J. Carrete, N. Mingo, D. Broido, Mater. Today Phys. 1 (2017) 31.
[18] T. Wang, Z. Gui, A. Janotti, C. Ni, P. Karandikar, Phys. Rev. Mater. 1 (2017): 034601.
[19] B. Dongre, J. Carrete, S. Wen, J. Ma, W. Li, N. Mingo, G.K.H. Madsen, J. Mater. Chem. A 8 (2020) 1273.
[20] A. Katre, J. Carrete, B. Dongre, G.K.H. Madsen, N. Mingo, Phys. Rev. Lett. 119 (2017): 075902.
[21] W. Li, J. Carrete, N.A. Katcho, N. Mingo, Comput. Phys. Commun. 185 (2014) 1747.
[22] A. Kundu, X. Yang, J. Ma, T. Feng, J. Carrete, X. Ruan, G.K.H. Madsen, W. Li, Phys. Rev. Lett. 126 (2021): 115901.
[23] B. Liao, B. Qiu, J. Zhou, S. Huberman, K. Esfarjani, G. Chen, Phys. Rev. Lett. 114 (2015): 115901.
[24] S. Wen, J. Ma, A. Kundu, W. Li, Phys. Rev. B 102 (2020): 064303.
[25] F. Giustino, Rev. Mod. Phys. 89 (2017): 015003.
[26] J. Berges, N. Girotto, T. Wehling, N. Marzari, S. Poncé, Phys. Rev. X 13 (2023): 041009.
[27] M. Calandra, G. Profeta, F. Mauri, Phys. Rev. B 82 (2010): 165111.
[28] A. Marini, Phys. Rev. B 107 (2023): 024305.
[29] F. Macheda, P. Barone, F. Mauri, Phys. Rev. Lett. 129 (2022): 185902.
[30] N.H. Protik, C. Li, M. Pruneda, D. Broido, P. Ordejón, npj Comput. Mater. 8 (2022) 28.
[31] Y. Quan, Y. Chen, B. Liao, Phys. Rev. B 107 (2023): 245202.
[32] N.H. Protik, D.A. Broido, Phys. Rev. B 101 (2020): 075202.
[33] N.H. Protik, B. Kozinsky, Phys. Rev. B 102 (2020): 245202.
[34] Y. Chen, J. Ma, W. Li, Phys. Rev. B 99 (2019) 1.
[35] N. Mingo, K. Esfarjani, D.A. Broido, D.A. Stewart, Phys. Rev. B 81 (2010): 045408.
[36] E.N. Economou, Green's Functions in Quantum Physics, vol. 7, Springer Science & Business Media, 2006.
[37] M. Fava, N.H. Protik, C. Li, N.K. Ravichandran, A.R. J Carrete, G.K.H. Madsen, N. Mingo, D. Broido, npj Comput. Mater. 7 (2021) 54.
[38] J. Ma, S.-H. Wei, T. Gessert, K.K. Chin, Phys. Rev. B 83 (2011): 245207.
[39] J. Kono, S. Takeyama, H. Yokoi, N. Miura, M. Yamanaka, M. Shinohara, K. Ikoma, Phys. Rev. B 48 (1993): 10909.
[40] N.T. Son, O. Kordina, A.O. Konstantinov, W.M. Chen, E. Sörman, B. Monemar, E. Janzén, Appl. Phys. Lett. 65 (1994) 3209.
[41] U. Lindefelt, J. Appl. Phys. 84 (1998) 2628.
[42] J. Buckeridge, Comput. Phys. Commun. 244 (2019) 329.
[43] H. Kuwabara, S. Yamada, Phys. Status Solidi A 30 (1975) 739.
[44] Y. Zhou, W. Li, M. Wu, L.-D. Zhao, J. He, S.-H. Wei, L. Huang, Phys. Rev. B 97 (2018): 245202.
[45] N. Matsushima, J. Yamauchi, Jpn. J. Appl. Phys. 58 (2019(): 061005. "natexlaba).
[46] W. Windl, A. Demkov, MRS Online Proc. Libr. 510 (1998) 181.
[47] A. Fukumoto, Phys. Rev. B 53 (1996) 4458.
[48] N. Matsushima, J. Yamauchi, Jpn. J. Appl. Phys. 58 (2019): 031001 natexlabb).
[49] T. Fan, W. Liu, Z. Ruan, Y. Cao, T. Ye, J. Liu, F. Zhong, X. Tan, H. Liang, D. Chen, et al., J. Mater. 20 (2022) 3633.
[50] J. Bernholc, S. Kajihara, C. Wang, A. Antonelli, R. Davis, Mater. Sci. Eng. B 11 (1992) 265.
[51] C. Wang, J. Bernholc, R. Davis, Phys. Rev. B 38 (1988): 12752.
[52] J. Xi, B. Liu, Y. Zhang, W.J. Weber, Comput. Mater. Sci." "textbf 123 (2016) 131.
[53] P.A. Schultz, R.M. Van Ginhoven, A.H. Edwards, Phys. Rev. B" "textbf 103 (2021): 195202.
[54] L. Torpo, S. Pöykkö, R.M. Nieminen, Phys. Rev. B 57 (1998) 6243.
[55] G. Kresse, J. Furthmüller, Comput. Mater. Sci. 6 (1996) 15.
[56] See Supplemental Material for more details on band structure, phonon dispersion, the convergence test of ph-def scattering rates and the computational details of 4H-SiC, including Refs. [70, 71].
[57] D. Bimberg, M. Altarelli, N. Lipari, Solid State Commun. 40 (1981) 437.
[58] A.J. Cohen, P. Mori-Sánchez, W. Yang, Science 321 (2008() 792. "natexlaba).
[59] A.J. Cohen, P. Mori-Sánchez, W. Yang, Phys. Rev. B 77 (2008(): 115123. "natexlabb)).
[60] A. Togo, I. Tanaka, Scripta Mater. 108 (2015) 1.
[61] J. Serrano, J. Strempfer, M. Cardona, M. Schwoerer-Böhning, H. Requardt, M. Lorenzen, B. Stojetz, P. Pavone, W. Choyke, Appl. Phys. Lett. 80 (2002) 4360.
[62] F. Widulle, T. Ruf, O. Buresch, A. Debernardi, M. Cardona, Phys. Rev. Lett. 82 (1999) 3089.
[63] J.P. Perdew, K. Burke, M. Ernzerhof, Phys. Rev. Lett. 77 (1996) 3865.
[64] J. Carrete, B. Vermeersch, A. Katre, A. van Roekeghem, T. Wang, G.K.H. Madsen, N. Mingo, Comput. Phys. Commun. 220 (2017) 351.
[65] B. Dongre, J. Carrete, A. Katre, N. Mingo, G.K.H. Madsen, J. Mater. Chem. C 6 (2018) 4691.
[66] P. Giannozzi, O. Andreussi, T. Brumme, O. Bunau, M.B. Nardelli, M. Calandra, R. Car, C. Cavazzoni, D. Ceresoli, M. Cococcioni, et al., J. Phys. Condens. Matter 29 (2017): 465901.
[67] S. Poncé, E.R. Margine, C. Verdi, F. Giustino, Comput. Phys. Commun. 209 (2016) 116.
[68] A. Kundu, F. Otte, J. Carrete, P. Erhart, W. Li, N. Mingo, G.K.H. Madsen, Phys. Rev. Mater. 3 (2019): 094602.
[69] N. Son, W. Chen, O. Kordina, A. Konstantinov, B. Monemar, E. Janzén, D. Hofman, D. Volm, M. Drechsler, B. Meyer, Appl. Phys. Lett. 66 (1995) 1074.
[70] W. Choyke, D. Hamilton, L. Patrick, Phys. Rev. 133 (1964) A1163.
[71] M. Ikeda, H. Matsunami, T. Tanaka, Phys. Rev. B 22 (1980) 2842.